

# Highly Selective Gas Sensors Based on Graphene Nanoribbons Grown by Chemical Vapor Deposition

Mikhail Shekhirev, Alexey Lipatov, Angel Torres, Nataliia S. Vorobeva, Ashley Harkleroad, Andrey Lashkov, Victor Sysoev, and Alexander Sinitskii\*



Cite This: *ACS Appl. Mater. Interfaces* 2020, 12, 7392–7402



Read Online

ACCESS |



Metrics & More



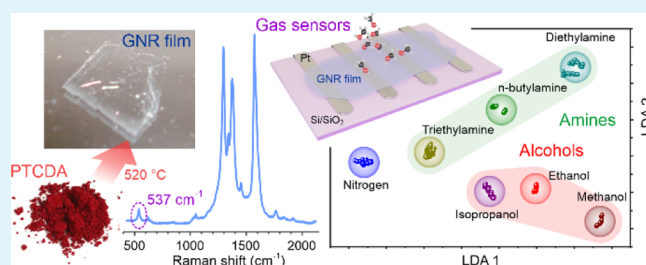
Article Recommendations



Supporting Information

**ABSTRACT:** Despite the recent advances in bottom-up synthesis of different kinds of atomically precise graphene nanoribbons (GNRs) with very diverse physical properties, the translation of these GNRs into electronic devices remains challenging. Among other factors, the electronic characterization of GNRs is hampered by their complex synthesis that often requires custom-made organic precursors and the need for their transfer to dielectric substrates compatible with the conventional device fabrication procedures. In this paper, we demonstrate that uniform electrically conductive GNR films can be grown on arbitrary high-temperature-resistant substrates, such as metals, Si/SiO<sub>2</sub>, or silica glasses, by a simple chemical vapor deposition (CVD) approach based on thermal decomposition of commercially available perylenetetracarboxylic dianhydride molecules. The results of spectroscopic and microscopic characterization of the CVD-grown films were consistent with the formation of oxygen-terminated  $N = 5$  armchair GNRs. The CVD-grown nanoribbon films exhibited an ambipolar electric field effect and low on–off ratios, which were in agreement with the predicted metallic properties of  $N = 5$  armchair GNRs, and remarkable gas sensing properties to a variety of volatile organic compounds (VOCs). We fabricated a GNR-based electronic nose system that could reliably recognize VOCs from different chemical classes including alcohols (methanol, ethanol, and isopropanol) and amines (*n*-butylamine, diethylamine, and triethylamine). The simplicity of the described CVD approach and its compatibility with the conventional device fabrication procedures, as well as the demonstrated sensitivity of the GNR devices to a variety of VOCs, warrant further investigation of CVD-grown nanoribbons for sensing applications.

**KEYWORDS:** graphene nanoribbons, bottom-up synthesis, chemical vapor deposition, perylenetetracarboxylic dianhydride (PTCDA), gas sensors, electronic nose



## INTRODUCTION

Because of their highly tunable physical properties,<sup>1</sup> graphene nanoribbons (GNRs) show a great promise for electronic and optoelectronic applications. Over the last decade, considerable efforts have been devoted to the development of bottom-up synthetic approaches to atomically precise GNRs.<sup>2,3</sup> Most bottom-up approaches can be classified into two major categories: (1) on-surface methods that produce GNRs on coinage metal substrates in ultrahigh vacuum (UHV) conditions<sup>4–12</sup> and (2) solution methods that rely on polymerization procedures using Yamamoto,<sup>13–15</sup> Suzuki–Miyaura,<sup>16,17</sup> or Diels–Alder<sup>18</sup> reactions and oxidative cyclo-dehydrogenation of the resulting polymers.<sup>13–18</sup>

While a number of GNRs with very diverse structures and properties have been demonstrated in recent years by both on-surface and solution approaches,<sup>2–18</sup> the effective translation of nanoribbons to devices remains a serious challenge. Among other issues, neither on-surface nor solution-based approaches enable the synthesis of GNRs directly on substrates compatible with device fabrication, such as Si/SiO<sub>2</sub>, and laborious

procedures for a transfer of nanoribbons to proper substrates are in order.<sup>19</sup> For example, we recently reported a procedure for self-assembly of solution-synthesized GNRs into uniform thin films<sup>20</sup> and employed it to fabricate highly sensitive and selective GNR-based gas sensors.<sup>21</sup> While the final device structures were shown to be very attractive for gas sensing, if viewed from the application standpoint, their preparation is laborious and expensive as it involves a multistep synthesis of atomically precise nanoribbons,<sup>21</sup> a use of highly corrosive chlorosulfonic acid for the GNR self-assembly,<sup>20</sup> and a manual transfer of GNR films to substrates with prepatterned electrodes.<sup>21</sup> Likewise, the recent efforts to translate the on-surface synthesized GNRs into electronic devices involved the GNR growth from specially synthesized molecular precursors

**Received:** August 5, 2019

**Accepted:** January 13, 2020

**Published:** February 3, 2020

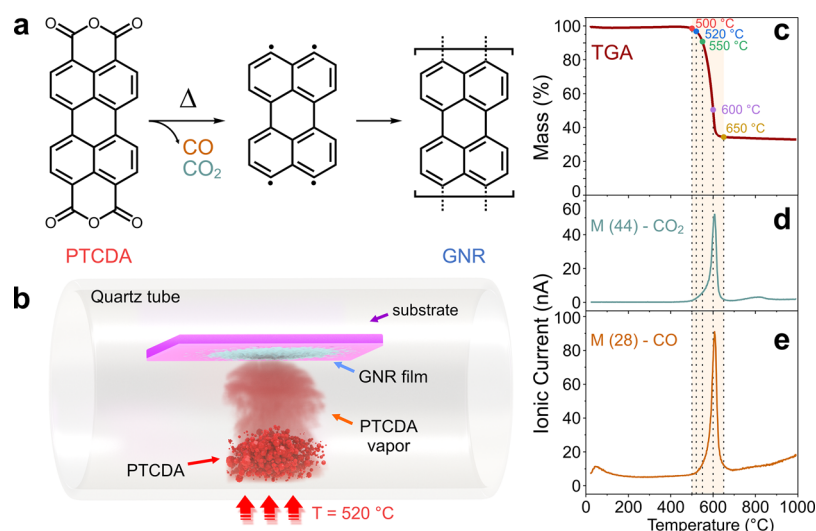


**Figure 1.** GNR synthesis. (a) Scheme of the thermal decomposition of PTCDA. (b) Scheme of the CVD synthesis of a GNR film. The PTCDA powder was heated in a furnace tube to initiate the molecule decomposition and the formation of GNRs that deposited on the substrate. (c) TGA curve for PTCDA measured in Ar (1 atm) from room temperature to 1000 °C at a heating rate of 10 °C/min. (d,e) Mass spectrometry data for the atomic mass units of (d) 44/CO<sub>2</sub> and (e) 28/CO.

in UHV conditions on expensive sacrificial Au(111) substrates that were dissolved during the manual transfer of nanoribbons to Si/SiO<sub>2</sub> wafers for device fabrication.<sup>19</sup> Thus, the purpose of this study was to develop a procedure for the growth of electrically conductive GNR films (1) from an inexpensive commercially available molecule, eliminating the need for a laborious organic synthesis of specially designed GNR precursors, (2) without the use of expensive UHV equipment, and (3) directly on dielectric substrates, such as Si/SiO<sub>2</sub>, eliminating the need for a manual transfer of nanoribbons and enabling immediate device fabrication.

In this paper, we demonstrate a GNR growth approach that satisfies all these criteria. We employed a well-known reaction of thermal decomposition of commercially available perylene-tetracarboxylic dianhydride (PTCDA) molecule (Figure 1a), which was extensively studied in the past.<sup>22–42</sup> The thermal elimination of the dianhydride groups in the form of CO and CO<sub>2</sub> from the PTCDA molecules results in the formation of perylene tetraradicals, which then polymerize and form nanoribbons; the mechanism of the decomposition was intensively studied by various methods and is shown in Figure 1a.<sup>34,38</sup> The first step of this mechanism is thermally activated, which allows synthesis of the GNR-based fibers or conductive films independent of metal substrates.<sup>22–42</sup>

We demonstrate that the PTCDA-derived GNR films can be grown directly on dielectric substrates in an inexpensive homemade chemical vapor deposition (CVD) system and employed for device fabrication and electrical measurements. Similar to the solution-synthesized GNRs,<sup>21</sup> the CVD-grown GNR films are shown to have remarkable gas sensing properties to a variety of volatile organic compounds including alcohols (methanol, ethanol, and isopropanol) and amines (*n*-butylamine, diethylamine, and triethylamine). Furthermore, we fabricated a GNR multisensor array that could reliably discriminate these analytes using an electronic nose (e-nose) approach. Together with other theoretical<sup>43–45</sup> and experimental studies<sup>21,46</sup> on nanoribbon-based sensors, this work is expected to stimulate further investigation of bottom-up synthesized GNRs for sensing applications.

## RESULTS AND DISCUSSION

The synthesis of GNR films was adapted from the previously published CVD techniques.<sup>24,34–37</sup> In our experiments, the deposition was performed by heating the PTCDA powder located directly below the substrate in a homemade CVD system under different conditions (temperature, pressure, and time), as demonstrated in Figure 1b. Unlike other recently published approaches for the CVD growth of GNRs<sup>47–50</sup> that employed the same Ullmann-like coupling reactions on gold substrates as in prior studies on the on-surface synthesis of nanoribbons in UHV conditions,<sup>4–7</sup> the approach described here can be implemented directly on dielectric substrates and is not limited to a GNR monolayer but can rather produce multilayer films.

In order to determine the temperature range, in which the coupling reaction according to the mechanism shown in Figure 1a is expected, we performed thermogravimetric analysis (TGA) of PTCDA combined with mass spectrometry of evolving gases (Figure 1c–e). The measurements were performed in the argon atmosphere at  $p(\text{Ar}) = 1$  atm, and the PTCDA powder was heated from room temperature to 1000 °C at a heating rate of 10 °C/min. A number of previous studies focused on PTCDA crystals grown by high-vacuum molecular sublimation at about 400 °C.<sup>51</sup> Our data show that at this temperature and at  $p(\text{Ar}) = 1$  atm, PTCDA remains stable; that is, it does not sublime and no evolving gases indicative of the molecular decomposition are detected. A rapid mass loss starts at about 500 °C (Figure 1c), and it corresponds not only to the sublimation but also the decomposition of PTCDA according to the mechanism shown in Figure 1a, as the evolution of both CO<sub>2</sub> (Figure 1d) and CO (Figure 1e) is observed. The correlated mass loss and CO/CO<sub>2</sub> evolution end when the temperature reaches approximately 650 °C (Figure 1c–e). Overall, the data presented in Figure 1c–e are in agreement with the mechanism shown in Figure 1a and suggest that the GNR growth should be investigated in the temperature range from 500 to 650 °C.

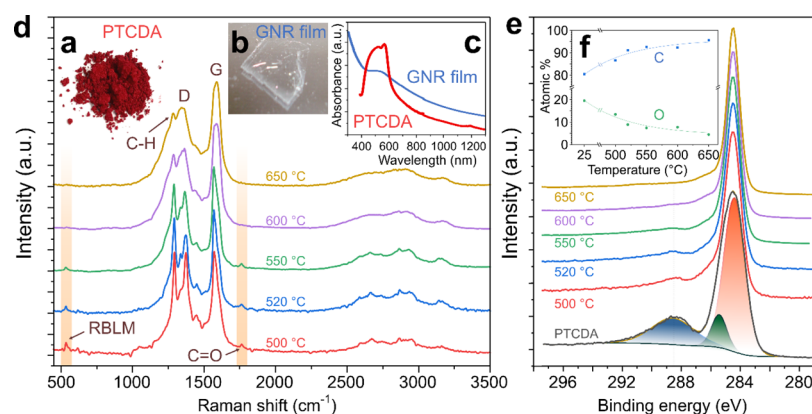


**Figure 2.** Spectroscopic characterization of GNR films grown at different temperatures. (a,b) Optical photographs of (a) PTCDA powder and (b) a GNR film grown at 520 °C. (c) Optical absorbance spectra of PTCDA and the GNR film shown in (b). (d) Raman spectra of GNR films grown on Au foils at 500, 520, 550, 600, and 650 °C. (e) XPS C 1s spectra of PTCDA and GNR films grown on Au foils at 500, 520, 550, 600, and 650 °C. (f) XPS-derived composition of GNR films grown on Au foils at different temperatures. The 25 °C data points show experimental XPS results for pure PTCDA, for which the theoretical C:O ratio is 4:1. The lines are a guide for the eye.

In order to investigate the GNR deposition process, we selected five different temperatures in the 500–650 °C range and used them to grow nanoribbons on Au foils, which were used to exclude the presence of substrate-related oxygen for the composition analysis of GNR films by X-ray photoelectron spectroscopy (XPS). As shown in Figure 1c–e, 500, 520, and 550 °C represent early stages of PTCDA decomposition, 600 °C corresponds to the maximum rates of CO and CO<sub>2</sub> evolution, while at 650 °C, the thermal decomposition of PTCDA is complete.

All grown films were visually different from the PTCDA precursor, which is a bright red powder (Figure 2a). In contrast, the GNR films were transparent and exhibited a grayish tint, as shown for the film that was grown at 520 °C and transferred from Si/SiO<sub>2</sub> to a glass substrate. UV–vis–near-infrared (NIR) spectra of the GNR films grown in this work (Figure 2c) show an overall monotonous optical absorption decrease from the UV to the NIR region with a step-like feature around 600 nm. Interestingly, very similar spectra were previously reported for the solution-synthesized GNRs with the same poly-peri-naphthalene aromatic core.<sup>52</sup> On the contrary, PTCDA molecules have a very strong absorbance in the visible range of spectrum, which is responsible for their color (Figure 2c).

Figure 2d shows the Raman spectra of GNR films grown at different temperatures. These spectra are very similar to the ones reported in the syntheses of poly-peri-naphthalene samples using CVD or laser ablation techniques<sup>22,23,26,27,30–32,37,40,41</sup> and contain highly intense G (1573 cm<sup>−1</sup>), D (1374 cm<sup>−1</sup>), and edge C–H (1294 cm<sup>−1</sup>) bands, as well as several smaller bands, among which of particular importance for the following discussion will be the peaks at 537 and 1774 cm<sup>−1</sup>. The peak at 537 cm<sup>−1</sup> represents the radial breathing-like mode (RBLM) of 5-AGNRs and is in good agreement with theoretical predictions<sup>53,54</sup> and the experimental data previously reported for 5-AGNRs.<sup>50</sup> This peak also exists in the Raman spectra of PTCDA molecules,<sup>55</sup> which have the same width as 5-AGNRs. The peak at 1774 cm<sup>−1</sup> corresponds to the C=O breathing mode<sup>55,56</sup> and represents the residual oxygen functionalities because of the incomplete decomposition of PTCDA.

The oxygen content in the GNR films grown on Au foils was probed by XPS. Figure 2e shows a reference XPS C 1s spectrum of PTCDA, which was deconvoluted using three

components with the most intense peak at 284.5 eV corresponding to the sp<sup>2</sup>-hybridized carbon atoms and smaller peaks at 286.1 and 289.2 eV representing carbon atoms in the  $\pi$  system and O=C–O functionalities.<sup>42</sup> For the GNR films, the peaks related to the oxygen-bound carbon atoms, especially the peak at 288.4 eV, visibly decrease in intensity with the increasing growth temperature (Figure 2e). The increase in the C:O atomic ratio with the temperature is illustrated by Figure 2f. For the pristine PTCDA molecule, the theoretical C:O ratio is 4:1, and based on the XPS results, the sample contained 80.5 at. % of carbon and 19.5 at. % of oxygen, while the chemical composition of the GNR films grown at 650 °C was C (95.5 at. %) and O (4.5 at. %).

Overall, the results of TGA, mass spectrometry, Raman spectroscopy, and XPS collectively provide the following picture of the PTCDA decomposition and GNR growth. The sublimation and decomposition of molecules start at about 500 °C. At this temperature, GNR films that are visually different from the PTCDA precursor can already form on various substrates. These films contain a considerable amount of the residual oxygen functionalities that likely terminate the ribbons, which is evidenced by the continuous evolution of CO and CO<sub>2</sub> at higher temperatures (Figure 1d,e), the presence of the C=O breathing mode at 1774 cm<sup>−1</sup> in the Raman spectra (Figure 2d), and the XPS data (Figure 2e,f). Based on the mass spectrometry and XPS results, the oxygen content decreases with temperature, and in the range from 550 to 600 °C the C=O band disappears from the Raman spectra (Figure 2d). However, the RBLM mode disappears in the same temperature range as well, while the D and G bands visibly broaden. These observations indicate that while GNR films graphitize, they become more disordered. Based on these observations, we focused further investigation on the films grown in the 500–550 °C temperature, which likely contained shorter but more crystalline GNRs with oxygen terminations. Considering that the Raman spectra of the films grown at 520 °C show sharper and better-defined peaks than the spectra of GNRs grown at other temperatures, these samples were selected for the device and sensor measurements. It should also be noted that for the depositions performed at temperatures below 520 °C, we often observed nonuniform isolated GNR islands on substrates, which can be explained by low PTCDA sublimation rates (Figure 1c).



As we discuss above, the PTCDA deposition at 600 °C or higher temperatures resulted in a structural degradation of GNRs based on the results of Raman spectroscopy (Figure 2d). Similarly, the quality of Raman spectra degraded if the GNRs that were originally grown at 520 °C were then annealed at 600 °C (Figure S1a). As previously suggested, higher temperatures may result in the cross-fusion of nanoribbons forming wider graphitic structures.<sup>35</sup>

While some metals were found to catalyze the PTCDA decomposition and promote the film growth,<sup>37</sup> in general, the process does not require a metal substrate. As a result, the deposition could be performed on almost any substrate that is stable at high temperatures, including Si/SiO<sub>2</sub> wafers, metals (e.g., Cu and Au foils), mica, and quartz slides. No special pretreatment was required for the substrates used for the GNR growth experiments. It should be mentioned that substrates play an important role in the Ullmann-like coupling reactions that are widely used for the on-surface synthesis of GNRs.<sup>4–12</sup> For example, Cu(111) is known to be more reactive than the more commonly used Au(111) and enables growing GNRs at considerably lower temperatures.<sup>57,58</sup> However, we did not observe any differences between the Raman spectra of the GNR films grown at 520 °C on metal substrates (Au, Cu) and SiO<sub>2</sub> (Figure S1b), suggesting that the nature of the substrate is not a very important factor for the PTCDA decomposition reaction (Figure 1a). Furthermore, we did not observe any significant difference between the Raman spectra of GNRs grown for different times (for instance, 10 min vs 30 min, see Figure S1c), although the film thickness increased with the deposition time. All the following electrical measurements were performed on the GNR films grown on Si/SiO<sub>2</sub> at 520 °C for 30 min under 1 atm of Ar. According to the XPS results, these films had the following chemical composition: C (91.1 at. %) and O (8.9 at. %).

A representative Raman spectrum of the CVD-grown GNR film on Si/SiO<sub>2</sub> that was used for the device and sensor measurements is shown in Figure 3a; it is consistent with the spectrum shown in Figure 2d for the film grown on Au foil. Of practical importance is the fact that during the deposition, a

GNR film is uniformly covering the entire exposed surface of a substrate. Furthermore, scanning electron microscopy (SEM) studies reveal that the GNR films are also uniform on the micrometer scale (Figure 3b). On the sub-100 nm scale, however, the grain structure of the GNR films becomes visible in the atomic force microscopy (AFM) images (Figure 3c). An AFM height profile measured for the GNR film shown in Figure 3c reveals that it had a thickness of about 7 nm. Because of the rough surfaces of the CVD-grown GNR films, their considerable thickness, and polycrystalline nature, as well as the postgrowth handling of samples in ambient conditions, which resulted in the presence of surface adsorbates, visualization of nanoribbons by scanning tunneling microscopy, which is a commonly used characterization technique in GNR studies,<sup>3–12</sup> was very challenging. We employed transmission electron microscopy (TEM), which further confirmed the polycrystalline structure of the GNR films. Figure 3d shows one of the GNR grains that is about 15 nm in size and consists of linear structures that are densely packed with a periodicity of about 0.32 nm, which is close to the interlayer distance in graphite (0.34 nm) and the distances of  $\pi$ - $\pi$  stacking observed for assemblies of graphitic materials.

Because the GNR films could be grown on insulating substrates, they could be directly used for patterning and device fabrication without any additional transfer steps, which is different from other nanoribbons grown by CVD on gold substrates.<sup>47–50</sup> We first deposited a nanoribbon film on a heavily p-doped Si substrate passivated with a 300 nm-thick layer of SiO<sub>2</sub>, and then used e-beam lithography (EBL) and reactive ion etching (RIE) to pattern isolated 15  $\mu$ m-wide GNR strips. Then, we used a second-step EBL and electron beam evaporation to create metal contacts to the GNR strips consisting of 15 nm of Au on top of a 3 nm adhesion layer of Cr. The optical photograph of an array of 25 field-effect transistor (FET) devices is shown in Figure 4a, and the SEM image of a representative device is shown in Figure 4b. In the electrical measurements, the Cr/Au pads served as source (S) and drain (D) electrodes, while the heavily p-doped Si substrate served as a bottom gate (G).

Figure 4c,d summarizes the results of room-temperature electrical measurements of the GNR devices. The ribbons that are expected to form in the described CVD process (Figure 1a,b) are  $N = 5$  armchair GNRs that are theoretically predicted to have a small electronic band gap,<sup>59</sup> which was confirmed by scanning tunneling spectroscopy on Au(111).<sup>6</sup> All devices showed linear  $I_{DS}$ - $V_{DS}$  dependencies modulated by the gate voltage (Figure 4c) and an ambipolar field effect (Figure 4d). Because of their predicted small band gap, these GNRs were not expected to exhibit high on-off ratios in FET measurements (an average of 1.13), while low mobility values (the average values for all 25 devices are  $4.3 \times 10^{-4}$  and  $2.1 \times 10^{-4}$  cm<sup>2</sup> V<sup>-1</sup> s<sup>-1</sup> for holes and electrons, respectively) can be explained by the polycrystalline nature of the GNR films (Figure 3c,d). The measured GNR devices generally showed a small hysteresis of  $I_{DS}$ - $V_G$  dependence when the gate voltage was swept in the forward and reverse directions. While various species could contribute to hysteresis of electronic transport in devices based on carbon nanomaterials, such as carbon nanotubes<sup>60</sup> and graphene,<sup>61</sup> the adsorbed water molecules are often cited as one of the strongest causes. In our case, the small hysteresis could therefore be related to the hydrophobicity of the nanoribbons as well as their growth at high temperatures in an inert Ar atmosphere, ensuring the

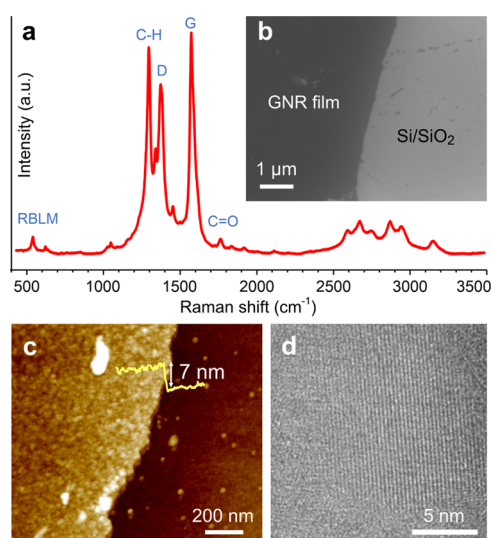


**Figure 3.** Characterization of the GNR films. (a) Raman spectrum of the GNRs grown on Si/SiO<sub>2</sub> at 520 °C. (b) SEM image of a GNR film on a Si/SiO<sub>2</sub> substrate. (c) AFM image of a GNR film on Si/SiO<sub>2</sub> with a corresponding height profile. (d) TEM image of GNRs.

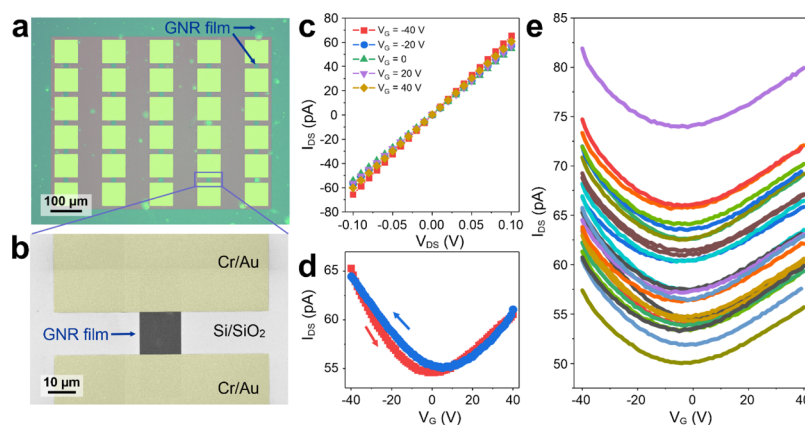


**Figure 4.** GNR-based FETs. (a) Optical photograph of an array of 25 GNR devices patterned from a CVD-grown film. (b) SEM image of one of the devices in the array. Cr/Au electrodes are colored for clarity. (c) Representative  $I_{DS}$ – $V_{DS}$  curves for one of the GNR devices measured at gate voltages ranging from –40 to 40 V. (d)  $I_{DS}$ – $V_G$  curves measured for the same device as in (c) for forward and reverse  $V_G$  sweeps. (e)  $I_{DS}$ – $V_G$  curves for all 25 GNR FETs shown in (a) demonstrating the consistency of electronic properties of the devices in the array.

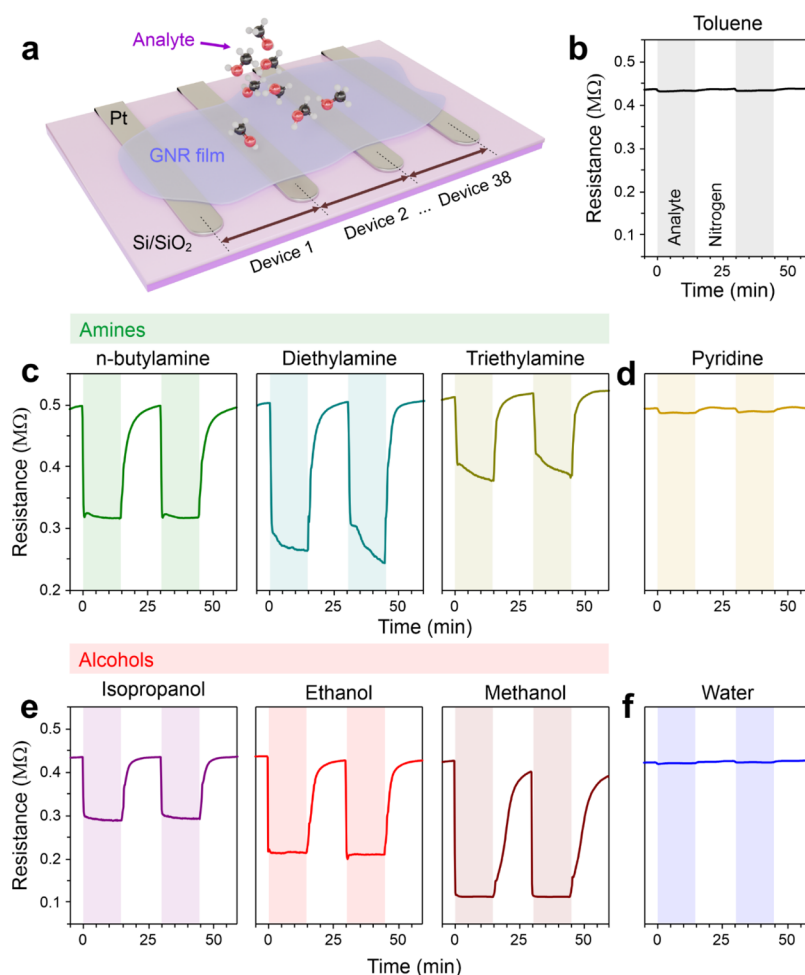


**Figure 5.** Sensors based on CVD-grown GNR films. (a) Scheme of the multisensor array. (b–f) Sensor responses of a representative GNR device in the array to selected gas analytes.

desorption of the water molecules from the Si/SiO<sub>2</sub> substrate prior to the GNR deposition. As shown in Figure 4e, all 25 devices exhibited very consistent transfer characteristics, suggesting the structural uniformity of the CVD-grown GNR films.

Encouraged by the remarkable gas sensing properties recently found in the self-assembled films of solution-

synthesized GNRs,<sup>21</sup> we performed sensor measurements on the CVD-grown GNR films as well. Despite the interest in GNR sensors from theoretical standpoint,<sup>43–45</sup> there are still only a limited number of experimental attempts to realize gas sensing devices based on bottom-up synthesized nanoribbons.<sup>21,46</sup> We deposited GNRs directly on a multielectrode chip that was similar to those used in our prior studies of

sensor properties of reduced graphene oxide (rGO),<sup>62</sup> graphene,<sup>63</sup> and GNRs<sup>21</sup> and consisted of a Si/SiO<sub>2</sub> substrate with 39 Pt electrodes (100 × 3000 μm<sup>2</sup> each) separated by ~70 μm gaps. Each pair of adjacent Pt electrodes bridged by a GNR film constituted a sensing device. Upon the nanoribbon growth, the chip thus contained 38 GNR sensors (Figure 5a) that could be measured independently of each other. The multielectrode chip also contained four independent Pt heaters that could be used to uniformly heat the device array or produce a temperature gradient across it, as well as two Pt thermoresistors for temperature measurements.

The responses of the GNR film to different analytes were measured using a homebuilt setup described in Supporting Information Note 3 and our previous publications.<sup>21,62,63</sup> Unlike our previous sensor study of solution-synthesized GNRs where we only tested their responses to low-molecular-weight alcohols,<sup>21</sup> here we expanded the scope of analytes to a series of amines (*n*-butylamine, diethylamine, and triethylamine) as well as toluene and pyridine. In the sensor measurements, the concentrations of all analytes were equal to 500 ppm.

We found that the sensor responses of GNR devices increased with temperature, and the behavior of a representative device in the multisensor array measured at 180 °C is shown in Figure 5b–f. The sensor responses were stable and reproducible with no substantial drift of a baseline, as further illustrated by the additional sensor data in Figure S3. In general, the effects of donor and acceptor molecules on the in-plane conductivity of a GNR device are similar to the applications of positive and negative gate voltages, respectively. Because the undoped GNR films show an ambipolar field effect with the conductivity minimum at a  $V_G$  of about 0 V (Figure 4d), adsorption of molecules of either kind (which is equivalent to an application of a gate voltage of either polarity) is expected to increase the device conductivity. Correspondingly, all molecules tested in this study resulted in a decrease in the resistance of GNR sensors (Figure 5b–f). This result is different from the previously reported behavior of the gas sensors based on self-assembled films of solution-synthesized GNRs that showed a large resistance increase upon exposure to alcohol analytes.<sup>21</sup> The different gas sensing properties of the solution-synthesized GNRs can be explained by their large electronic band gap<sup>21</sup> compared to the CVD-grown GNRs prepared in this work, which are expected to be nearly metallic,<sup>6,59</sup> and their peculiar arrangement in the self-assembled films that facilitated the intercalation of analyte molecules between nanoribbons and the associated increase in the film resistance.<sup>21</sup> Overall, these results suggest that the large diversity of GNRs with highly tunable physical properties<sup>1</sup> can likely be translated into a large variety of gas sensors with very different characteristics and potential applications.

The devices based on CVD-grown GNRs exhibited visibly different responses to the tested analytes (Figure 5b–f), as summarized in Table 1. While density functional theory simulations can potentially elucidate the details of the electron transfer from these molecules to GNRs, the sensor results observed experimentally can mostly be rationalized based on the interplay of donor/acceptor properties as well as the size, shape, and related steric effects of the molecules. Toluene does not have strong donor/acceptor properties and shows a very weak sensor response experimentally (Figure 5b). Compared to toluene, the amine analytes show much stronger responses because of the electron donating effect of the nitrogen's lone

Table 1. Sensor Responses to Different Analytes

analyte	$ \Delta R /R_0$ , %	$R_0/R_{\text{gas}}$
<i>n</i> -butylamine	36.5	1.58
diethylamine	51.3	2.05
triethylamine	20.3	1.25
isopropanol	33.4	1.50
ethanol	51.1	2.04
methanol	73.6	3.8
toluene	1.2	1.01
pyridine	1.6	1.02
water	0.7	1.01

pair (Figure 5c). In this series, triethylamine shows a weaker response compared to *n*-butylamine and diethylamine because of its larger size and thus sterically hindered interaction between the lone pair on the nitrogen and the GNR film. The lone pair is available for such interaction with GNRs in both *n*-butylamine and diethylamine, but the latter, as a secondary amine, is a stronger electron donor and thus exhibits the strongest sensor response in the amine series (Figure 5c). In case of pyridine, it is expected to adsorb on graphene with its molecular plane parallel to the surface,<sup>64</sup> which weakens the electronic effect of the nitrogen's lone pair on GNR's conductivity and the associated sensor response (Figure 5d). Similar to amines, alcohols exhibited strong sensor responses that increased with decreasing the molecule size (Figure 5e). Unlike the extensively studied rGO sensors,<sup>62,65</sup> the GNR devices showed a weak sensor response to water molecules (Figure 5f). The sensitivity of rGO sensors to humidity is generally explained by the presence of abundant oxygen-containing surface functionalities that facilitate interaction between rGO and water via hydrogen bonding. Conversely, the hydrophobicity of GNRs could be responsible for their weak interaction with water molecules and thus the poor sensor response. From the practical point of view, a weak sensor response of the CVD-grown GNRs to humidity could be very beneficial because gas sensors operating in real environments often suffer from the detrimental effects of water as an interference analyte and an adsorbate affecting the chemisorption/surface reactions of other analytes. Overall, the GNR-based sensors show respectable sensitivity to alcohols and amines (Table 1), which, while still smaller than sensitivities found for self-assembled GNRs,<sup>21</sup> are significantly improved in comparison to graphene,<sup>63</sup> rGO,<sup>62</sup> graphene-based hybrid materials,<sup>66</sup> and other nanocarbon-based sensors.<sup>67</sup>

While each GNR sensor exhibited visibly different sensor responses to the tested molecules, which are varied by the magnitude and kinetics of the resistance change (Figure 5b–f), the selectivity of the analyte recognition can be significantly improved by processing the data from all devices in the multisensor array. We utilized the e-nose concept that employs digital signal processing of data from large arrays of nonidentical sensors and pattern recognition methods.<sup>68,69</sup> The e-nose systems are known for very high selectivity in analyte recognition. An e-nose system is first calibrated by exposing it to the molecules of interest and recording the characteristic patterns of sensor signals from individual devices in an analyte library. Then, in the following recognition experiments, the patterns of the measured sensor signals are compared with those recorded in the library and the analytes are identified.<sup>68,69</sup>



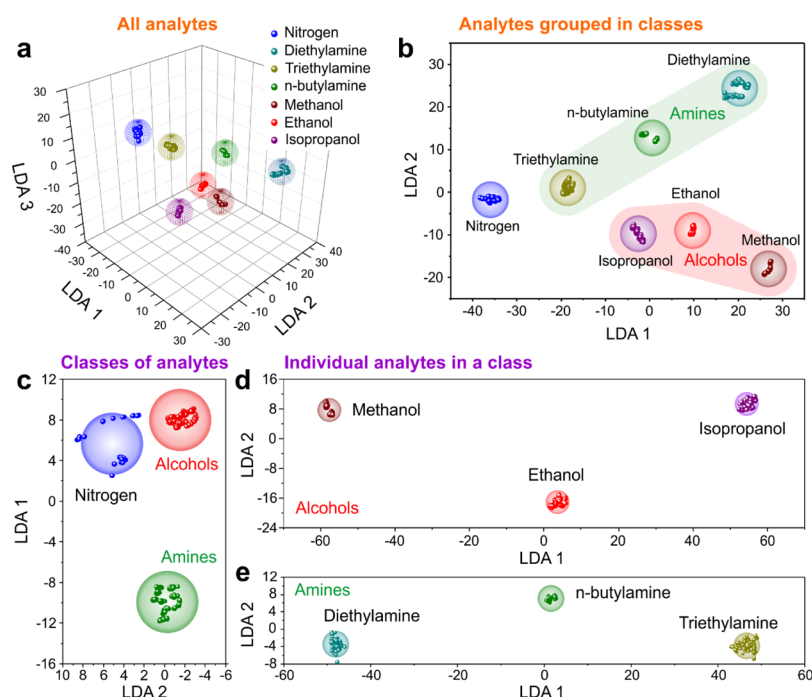


**Figure 6.** LDA analysis of the GNR-based multisensor array. Processing of chemiresistive response of GNR-based multisensor array using the LDA pattern recognition technique. (a) Recognition of the analyte-related LDA clusters in a three-component coordinate system showing all six analytes and nitrogen. (b) Recognition plane of the first two LDA components produced from panel (a). Analyte-related clusters are visually grouped into clearly distinguished areas corresponding to two chemical classes, alcohols (red) and amines (green). (c) Recognition plane prepared by processing the multisensor array responses recorded for all alcohols, all amines, and nitrogen gas as separate classes. Pure nitrogen is given as a background. Following the initial separation of the two analyte classes, the data within each class are further analyzed to distinguish the individual vapors as shown in the following panels. (d) Recognition plane prepared by processing the multisensor responses within the alcohol class, showing well-separated vector signals for methanol (dark red), ethanol (red), and isopropanol (purple). (e) Recognition plane prepared by processing the multisensor responses within the amine class, showing well-separated vector signals for diethylamine (blue green), triethylamine (olive), and *n*-butylamine (green). The analytes were mixed with nitrogen at 500 ppm concentration.

In the case of the GNR sensors in the array, while showing qualitatively similar sensing responses to the tested analytes, they exhibited a device-to-device variation that was likely caused by various morphological differences in the device channels (size and orientation of GNR domains, microscopic cracks, etc.) and was sufficiently large for an e-nose functionality. This device-to-device variation is illustrated by Figure S4, which shows the responses of six selected GNR devices in the array to the alcohol and amine analytes. Collectively, these responses compose characteristic patterns for each molecule as vector signals, which could be used for analyte recognition by this specific set of devices. To further increase the device-to-device variability, we used thermoresistors integrated in the sensor chip to induce a temperature gradient from 150 °C (device 1) to 200 °C (device 38) across the multisensor array so that each device operated at a slightly different temperature.<sup>70</sup>

In order to reliably discriminate the molecules and visualize the analyte recognition results, we used linear discriminant analysis (LDA).<sup>69</sup> We processed the data from all 38 GNR sensors in the array (Figure 5a) and focused on the discrimination of the alcohol and amine analytes, which showed the strongest sensor responses (Figure 5b–f). The LDA method transfers the multidimensional vector signals from the devices in the array into a reduced dimensional space in a way that maximizes the distances between class-related vectors and minimizes the scattering of the vector data corresponding to a single class. We employed three-component and two-component diagrams to visualize the

results of the LDA processing (Figure 6).<sup>69</sup> The points correspond to the multisensor vector data recorded using the GNR-based multisensor chip, while the spheres show the analyte-related clusters drawn with 0.99 probability around the cluster gravity centers. As shown in the three-dimensional diagram in Figure 6a, the analyte-related clusters are well separated, enabling reliable recognition of the analytes. The two-component LDA projection allows a simple discrimination of all tested analytes, and the responses could be visually grouped into separate areas of the LDA artificial space representing chemical classes of alcohols (red) or amines (green), see Figure 6b. To further improve the recognition of individual analytes, we suggest employing a hierarchical two-step approach to multisensor array signal analysis. First, all vector signals are analyzed by LDA using amines and alcohols as general targets, allowing separation of these two test analyte groups (Figure 6c). Second, further LDA analysis of the data for each group of analytes yields a confident distinction of chemically akin vapors. Figure 6d displays the recognition of alcohols (isopropanol, ethanol, and methanol), while Figure 6e shows the recognition of amines (diethylamine, triethylamine, and *n*-butylamine); in both cases LDA considered only the vector signals of analytes from the same group without accounting for other analytes. Note that the Euclidean distance between the cluster gravity centers within a chemical group (Figure 6d,e) is much larger than the distance between clusters when all analytes are analyzed together (Figure 6b), providing a more robust recognition of the analytes.

## CONCLUSIONS

In summary, we demonstrated that uniform electrically conductive GNR films can be grown on arbitrary substrates by a simple CVD approach based on thermal decomposition of inexpensive, commercially available PTCDA molecules. The results of spectroscopic and microscopic characterization of the CVD-grown films are consistent with the formation of  $N = 5$  armchair GNRs. The GNR films exhibit an ambipolar electric field effect and remarkable gas sensing properties to a variety of volatile organic compounds. We fabricated a GNR-based e-nose system that could reliably recognize analytes from different chemical classes including alcohols (methanol, ethanol, and isopropanol) and amines (*n*-butylamine, diethylamine, and triethylamine). The simplicity of the described CVD approach and its compatibility with the conventional device fabrication procedures, as well as the demonstrated sensitivity of the GNR devices to a variety of volatile organic compounds, warrant further investigation of CVD-grown nanoribbons for sensing applications.

## EXPERIMENTAL SECTION

**Materials and Methods.** PTCDA (98%) was purchased from Alfa Aesar and used as received without any additional purification. GNR films were grown on a variety of substrates, including 25  $\mu\text{m}$ -thick copper and gold foils (Alfa Aesar), heavily p-doped Si wafers with a 300 nm-thick layer of  $\text{SiO}_2$  (Silicon Quest International), V4-grade mica (SPI Supplies), or quartz slides using a homebuilt CVD system. Raman spectra of GNRs were recorded using a Thermo Scientific DXR Raman microscope with a 532 nm excitation laser. TGA and mass spectrometry were performed on a TA Instruments SDT 650 system that was equipped with a Discovery benchtop mass spectrometer. XPS was performed using a Thermo Scientific K-Alpha X-ray photoelectron spectrometer with monochromatic Al  $K\alpha$  (1486.6 eV) X-ray source. UV–vis–NIR spectroscopy was performed on a Jasco V-670 spectrophotometer. AFM analysis was performed on a Digital Instruments Nanoscope IIIa Dimension 3100 system using Bruker RTESPA AFM probes. SEM analysis was performed on a FEI Nova NanoSEM 450 scanning electron microscope. TEM images of GNRs were obtained using a FEI Tecnai Osiris transmission electron microscope.

**CVD Growth of GNRs.** The experimental setup is schematically shown in Figure 1b. Approximately 10 mg of PTCDA powder was placed in a quartz boat in the center of a quartz tube in a furnace (Lindberg Blue M). A substrate of choice (copper or gold foils, Si/ $\text{SiO}_2$ , mica, or quartz) was placed on top of the boat facing the PTCDA powder. The furnace was evacuated to the pressure of about 250 mTorr and then refilled with Ar to the pressure of up to 1 atm. Then, the furnace was heated to a selected temperature (500–650  $^\circ\text{C}$ ) for a certain time (10, 30, or 120 min). In the case of very low pressure ( $\sim 5$  mTorr), PTCDA sublimation occurs before the system reaches the decomposition temperature. This results in decomposition of a significant amount of PTCDA in the cold area of a tube, while only a very small amount of GNRs forms on a surface of interest.

**GNR Transfer.** For some experiments, the GNR films that were originally grown on Cu foils were transferred to various substrates. For AFM and SEM imaging, the ribbons were transferred from Cu to a Si/ $\text{SiO}_2$  substrate to visualize the sharp edge of a GNR film (Figure 3b,c). For TEM imaging, a GNR film was transferred to a TEM grid (lacey carbon on 300 mesh, no formvar, Ted Pella).

We employed the procedure that is widely used to transfer graphene from Cu to various substrates. For this, 4% polymethyl methacrylate (PMMA,  $M_w = 950,000$ ) solution in anisole was spin-coated over one side of a GNR-covered Cu foil and dried, and then, the other side of the Cu foil was treated by  $\text{O}_2$  RIE (Trion Minilock Phantom III). Then, the Cu foil was etched away with warm (50  $^\circ\text{C}$ ) 1 M  $\text{Fe}(\text{NO}_3)_3$  or  $\text{FeCl}_3$  aqueous solution. The remaining transparent

film was washed with deionized water to remove the etchant residues and transferred onto a substrate of choice. The substrate was dried and washed with acetone to remove PMMA.

**FET Device Fabrication and Measurements.** For electrical characterization, the films grown directly on a Si/ $\text{SiO}_2$  substrate were prepatterned via EBL and  $\text{O}_2$  RIE, and then Cr/Au contacts were deposited to fabricate the devices. EBL was performed using a Zeiss Supra 40 field-emission scanning electron microscope and a Raith pattern generator, while the metal deposition was performed using an AJA electron beam evaporation system. Electrical measurements were performed using a Lake Shore TTPX cryogenic probe station at the base pressure of  $2 \times 10^{-6}$  Torr. The device electrodes were connected to an Agilent 4155C semiconductor parameter analyzer that was linked to a computer through 82357B USB/GPIB interface and controlled using a National Instruments LabView code.

**Gas Sensor Measurements.** The detailed description of the gas sensing setup was published in our previous reports<sup>62,63</sup> and is described in Supporting Information Note 2. After purging the system with nitrogen gas, the chip with the deposited GNRs was gradually heated up to establish a temperature gradient across the array of devices from 150  $^\circ\text{C}$  on one edge of the chip to 200  $^\circ\text{C}$  on the other edge. The chip was annealed for about 1 h until there was no drift in the resistivity measurements of the GNR devices. The sensor measurements were performed exposing the multisensor chip to 500 ppm of an analyte for 15 min and purging it with pure nitrogen for another 15 min. Exposure-purge cycles were repeated three to five times for each analyte.

## ASSOCIATED CONTENT

### Supporting Information

The Supporting Information is available free of charge at <https://pubs.acs.org/doi/10.1021/acsami.9b13946>.

Raman spectra of GNRs synthesized at different temperatures, description of the setup for gas sensing measurements, and additional results of gas sensing measurements (PDF)

## AUTHOR INFORMATION

### Corresponding Author

Alexander Sinitskii – Department of Chemistry and Nebraska Center for Materials and Nanoscience, University of Nebraska–Lincoln, Lincoln, Nebraska 68588, United States; [orcid.org/0000-0002-8688-3451](https://orcid.org/0000-0002-8688-3451); Email: [sinitskii@unl.edu](mailto:sinitskii@unl.edu)

### Authors

Mikhail Shekhirev – Department of Chemistry, University of Nebraska–Lincoln, Lincoln, Nebraska 68588, United States; [orcid.org/0000-0002-8381-1276](https://orcid.org/0000-0002-8381-1276)

Alexey Lipatov – Department of Chemistry, University of Nebraska–Lincoln, Lincoln, Nebraska 68588, United States; [orcid.org/0000-0001-5043-1616](https://orcid.org/0000-0001-5043-1616)

Angel Torres – Department of Chemistry, University of Nebraska–Lincoln, Lincoln, Nebraska 68588, United States

Natalia S. Vorobeveva – Department of Chemistry, University of Nebraska–Lincoln, Lincoln, Nebraska 68588, United States

Ashley Harkleroad – Department of Chemistry, University of Nebraska–Lincoln, Lincoln, Nebraska 68588, United States

Andrey Lashkov – Department of Physics, Yuri Gagarin State Technical University, Saratov 410054, Russia

Victor Sysoev – Department of Physics, Yuri Gagarin State Technical University, Saratov 410054, Russia; National University of Science and Technology “MISiS”, Moscow 119991, Russia; [orcid.org/0000-0002-0372-1802](https://orcid.org/0000-0002-0372-1802)

Complete contact information is available at:

<https://pubs.acs.org/doi/10.1021/acsami.9b13946>



## Notes

The authors declare no competing financial interest.

## ■ ACKNOWLEDGMENTS

This work was supported by the National Science Foundation (NSF) through CHE-1455330. The work in MISiS was supported by the Ministry of Education and Science of the Russian Federation through grant K2-2018-014. A.L. and V.S. thank the Ministry of Education and Science of the Russian Federation for support by the grant no. 16.1119.2017/4.6. Some experiments were performed with the support of Nebraska Materials Research Science and Engineering Center (NSF DMR-1420645) using the instrumentation at Nebraska Nanoscale Facility, which is supported by the NSF (ECCS-1542182) and the Nebraska Research Initiative. A.H. was supported by the UNL Chemistry REU program through CHE-1757957.

## ■ REFERENCES

- (1) Yazyev, O. V. A Guide to the Design of Electronic Properties of Graphene Nanoribbons. *Acc. Chem. Res.* **2013**, *46*, 2319–2328.
- (2) Narita, A.; Chen, Z.; Chen, Q.; Müllen, K. Solution and On-Surface Synthesis of Structurally Defined Graphene Nanoribbons as a New Family of Semiconductors. *Chem. Sci.* **2019**, *10*, 964–975.
- (3) Clair, S.; de Oteyza, D. G. Controlling a Chemical Coupling Reaction on a Surface: Tools and Strategies for On-Surface Synthesis. *Chem. Rev.* **2019**, *119*, 4717–4776.
- (4) Cai, J.; Ruffieux, P.; Jaafar, R.; Bieri, M.; Braun, T.; Blankenburg, S.; Muoth, M.; Seitsonen, A. P.; Saleh, M.; Feng, X.; Müllen, K.; Fasel, R. Atomically Precise Bottom-Up Fabrication of Graphene Nanoribbons. *Nature* **2010**, *466*, 470–473.
- (5) Chen, Y.-C.; de Oteyza, D. G.; Pedramrazi, Z.; Chen, C.; Fischer, F. R.; Crommie, M. F. Tuning the Band Gap of Graphene Nanoribbons Synthesized from Molecular Precursors. *ACS Nano* **2013**, *7*, 6123–6128.
- (6) Kimouche, A.; Ervasti, M. M.; Drost, R.; Halonen, S.; Harju, A.; Joensuu, P. M.; Sainio, J.; Liljeroth, P. Ultra-Narrow Metallic Armchair Graphene Nanoribbons. *Nat. Commun.* **2015**, *6*, 10177.
- (7) Talirz, L.; Söde, H.; Dumschlaff, T.; Wang, S.; Sanchez-Valencia, J. R.; Liu, J.; Shinde, P.; Pignedoli, C. A.; Liang, L.; Meunier, V.; Plumb, N. C.; Shi, M.; Feng, X.; Narita, A.; Müllen, K.; Fasel, R.; Ruffieux, P. On-Surface Synthesis and Characterization of 9-Atom Wide Armchair Graphene Nanoribbons. *ACS Nano* **2017**, *11*, 1380–1388.
- (8) Ruffieux, P.; Wang, S.; Yang, B.; Sánchez-Sánchez, C.; Liu, J.; Dienel, T.; Talirz, L.; Shinde, P.; Pignedoli, C. A.; Passerone, D.; Dumschlaff, T.; Feng, X.; Müllen, K.; Fasel, R. On-Surface Synthesis of Graphene Nanoribbons with Zigzag Edge Topology. *Nature* **2016**, *531*, 489–492.
- (9) Rizzo, D. J.; Veber, G.; Cao, T.; Bronner, C.; Chen, T.; Zhao, F.; Rodriguez, H.; Louie, S. G.; Crommie, M. F.; Fischer, F. R. Topological Band Engineering of Graphene Nanoribbons. *Nature* **2018**, *560*, 204–208.
- (10) Gröning, O.; Wang, S.; Yao, X.; Pignedoli, C. A.; Borin Barin, G.; Daniels, C.; Cupo, A.; Meunier, V.; Feng, X.; Narita, A.; Müllen, K.; Ruffieux, P.; Fasel, R. Engineering of Robust Topological Quantum Phases in Graphene Nanoribbons. *Nature* **2018**, *560*, 209–213.
- (11) Moreno, C.; Vilas-Varela, M.; Kretz, B.; Garcia-Lekue, A.; Costache, M. V.; Paradinas, M.; Panighel, M.; Ceballos, G.; Valenzuela, S. O.; Peña, D.; Mugarza, A. Bottom-Up Synthesis of Multifunctional Nanoporous Graphene. *Science* **2018**, *360*, 199–203.
- (12) Shekhirev, M.; Zahl, P.; Sinitskii, A. Phenyl Functionalization of Atomically Precise Graphene Nanoribbons for Engineering Inter-ribbon Interactions and Graphene Nanopores. *ACS Nano* **2018**, *12*, 8662–8669.
- (13) Schwab, M. G.; Narita, A.; Hernandez, Y.; Balandina, T.; Mali, K. S.; De Feyter, S.; Feng, X.; Müllen, K. Structurally Defined Graphene Nanoribbons with High Lateral Extension. *J. Am. Chem. Soc.* **2012**, *134*, 18169–18172.
- (14) Vo, T. H.; Shekhirev, M.; Kunkel, D. A.; Orange, F.; Guinel, M. J.-F.; Enders, A.; Sinitskii, A. Bottom-Up Solution Synthesis of Narrow Nitrogen-Doped Graphene Nanoribbons. *Chem. Commun.* **2014**, *50*, 4172–4174.
- (15) Vo, T. H.; Perera, U. G. E.; Shekhirev, M.; Mehdi Pour, M.; Kunkel, D. A.; Lu, H.; Gruverman, A.; Sutter, E.; Cotlet, M.; Nykypanchuk, D.; Zahl, P.; Enders, A.; Sinitskii, A.; Sutter, P. Nitrogen-Doping Induced Self-Assembly of Graphene Nanoribbon-Based Two-Dimensional and Three-Dimensional Metamaterials. *Nano Lett.* **2015**, *15*, 5770–5777.
- (16) Yang, X.; Dou, X.; Rouhanipour, A.; Zhi, L.; Räder, H. J.; Müllen, K. Two-Dimensional Graphene Nanoribbons. *J. Am. Chem. Soc.* **2008**, *130*, 4216–4217.
- (17) Li, G.; Yoon, K.-Y.; Zhong, X.; Wang, J.; Zhang, R.; Guest, J. R.; Wen, J.; Zhu, X. Y.; Dong, G. A Modular Synthetic Approach for Band-Gap Engineering of Armchair Graphene Nanoribbons. *Nat. Commun.* **2018**, *9*, 1687.
- (18) Slota, M.; Keerthi, A.; Myers, W. K.; Tretyakov, E.; Baumgarten, M.; Ardavan, A.; Sadeghi, H.; Lambert, C. J.; Narita, A.; Müllen, K.; Bogani, L. Magnetic Edge States and Coherent Manipulation of Graphene Nanoribbons. *Nature* **2018**, *557*, 691–695.
- (19) Llinas, J. P.; Fairbrother, A.; Borin Barin, G.; Shi, W.; Lee, K.; Wu, S.; Yong Choi, B.; Braganza, R.; Lear, J.; Kau, N.; Choi, W.; Chen, C.; Pedramrazi, Z.; Dumschlaff, T.; Narita, A.; Feng, X.; Müllen, K.; Fischer, F.; Zettl, A.; Ruffieux, P.; Yablonovitch, E.; Crommie, M.; Fasel, R.; Bokor, J. Short-Channel Field-Effect Transistors with 9-Atom and 13-Atom Wide Graphene Nanoribbons. *Nat. Commun.* **2017**, *8*, 633.
- (20) Shekhirev, M.; Vo, T. H.; Mehdi Pour, M.; Lipatov, A.; Munukutla, S.; Lyding, J. W.; Sinitskii, A. Interfacial Self-Assembly of Atomically Precise Graphene Nanoribbons into Uniform Thin Films for Electronics Applications. *ACS Appl. Mater. Interfaces* **2017**, *9*, 693–700.
- (21) Mehdi Pour, M.; Lashkov, A.; Radocea, A.; Liu, X.; Sun, T.; Lipatov, A.; Korlacki, R. A.; Shekhirev, M.; Aluru, N. R.; Lyding, J. W.; Sysoev, V.; Sinitskii, A. Laterally Extended Atomically Precise Graphene Nanoribbons with Improved Electrical Conductivity for Efficient Gas Sensing. *Nat. Commun.* **2017**, *8*, 820.
- (22) Nishio, S.; Kanezawa, C.; Fukumura, H. Formation and Characterization of Polyperinaphthalenic Organic Semiconductor Nanoparticles by Laser Ablation of Mixture Targets of a Perylene Derivative with Cobalt Powder at 355 nm. *Appl. Phys. A: Mater. Sci. Process.* **2004**, *79*, 1449–1451.
- (23) Nishio, S.; Sato, H.; Yamabe, T. Control of Structure and Electric Properties of Amorphous Organic Semiconductive Thin Films Prepared by Excimer Laser Ablation. *Appl. Phys. A: Mater. Sci. Process.* **1999**, *69*, S711–S714.
- (24) Kaplan, M. L.; Schmidt, P. H.; Chen, C. H.; Walsh, W. M. Carbon Films with Relatively High Conductivity. *Appl. Phys. Lett.* **1980**, *36*, 867–869.
- (25) Murakami, M.; Yoshimura, S.; Iijima, S. Structural Properties of Graphitized Poly-Peri-Naphthalene Whiskers. *Appl. Phys. Lett.* **1986**, *48*, 390.
- (26) Yudasaka, M.; Tasaka, Y.; Tanaka, M.; Kamo, H.; Ohki, Y.; Usami, S.; Yoshimura, S. Polyperinaphthalene Film Formation by Pulsed Laser Deposition with a Target of Perylenetetracarboxylic Dianhydride. *Appl. Phys. Lett.* **1994**, *64*, 3237.
- (27) Nishio, S.; Mase, R.; Oba, T.; Matsuzaki, A.; Sato, H. Preparation of Amorphous Organic Semiconductor Thin Films with Polyperinaphthalene Structure on Temperature-Controlled Substrates by Excimer Laser Ablation of 3,4,9,10-Perylenetetracarboxylic Dianhydride. *Appl. Surf. Sci.* **1998**, *127–129*, 589–594.
- (28) Murthy, N. S.; Dantas, S. O.; Iqbal, Z.; Baughman, R. H. X-Ray Diffraction Evidence for the Formation of a Discotic Phase During Graphitization. *Carbon* **2001**, *39*, 809–813.
- (29) Murakami, M. Structural Properties of Graphitized Polyperinaphthalene Fiber. *J. Appl. Phys.* **1990**, *67*, 194–199.

- (30) Murakami, M.; Iijima, S.; Yoshimura, S. Morphology and Structure of a One-Dimensional Graphite Polymer, Poly-Peri-Naphthalene. *J. Appl. Phys.* **1986**, *60*, 3856.
- (31) Nishio, S.; Tamura, K.; Tsujine, Y.; Fukao, T.; Nakano, M.; Matsuzaki, A.; Sato, H.; Yamabe, T. Laser Ablation at 308 nm for the Mixture Target of 3,4,9,10-Perylenetetracarboxylic Dianhydride with Co Powder—Remarkable Enhancement on Elimination Efficiency of Anhydride Groups. *J. Photochem. Photobiol., A* **2001**, *145*, 165–171.
- (32) Nishio, S.; Kanezawa, C.; Fukumura, H. Effect of Cobalt Powder on Elimination Reaction of the Side Group of 3,4,9,10-Perylenetetracarboxylic Dianhydride During Laser Ablation at 355 nm. *J. Photopolym. Sci. Technol.* **2003**, *16*, 107–108.
- (33) Murakami, M.; Yoshimura, S. Synthesis of Poly-Peri-Naphthalene by Vapour-Phase Polymerization: an Approach to a One-Dimensional Graphite. *J. Chem. Soc., Chem. Commun.* **1984**, 1649–1650.
- (34) Iqbal, Z.; Ivory, D. M.; Marti, J.; Brédas, J. L.; Baughman, R. H. The Synthesis, Properties and Structure of Poly(Peri-Naphthalene): a Conducting, Undoped Organic Polymer. *Mol. Cryst. Liq. Cryst.* **1985**, *118*, 103–109.
- (35) Murakami, M.; Yoshimura, S. Synthesis of One-Dimensional Graphite Polymer, Poly-Peri-Naphthalene, by Vapor Phase Polymerization. *Mol. Cryst. Liq. Cryst.* **1985**, *118*, 95–102.
- (36) Iqbal, Z.; Maleysson, C.; Baughman, R. H. Electrical Conductivity of Pristine and Doped Polyperinaphthalene. *Synth. Met.* **1986**, *15*, 161–167.
- (37) Kamo, H.; Yudasaka, M.; Kurita, S.; Matsui, T.; Kikuchi, R.; Ohki, Y.; Yoshimura, S. Formation of Poly-Peri-Naphthalene Thin Film by Chemical Vapor Deposition. *Synth. Met.* **1994**, *68*, 61–63.
- (38) Murakami, M. Morphology and Polymerization Mechanism of One-Dimensional Graphite Polymer, Poly-Peri-Naphthalene. *Synth. Met.* **1987**, *18*, 531–536.
- (39) Tanaka, K.; Nishio, S.; Matsuura, Y.; Yamabe, T. Preparation of Organic Semiconductive Thin Film by Plasma-Polymerization of Aromatic Compounds and Their Derivatives. *Synth. Met.* **1993**, *55*, 896–901.
- (40) Yu, C.; Wang, S. C.; Sosnowski, M.; Iqbal, Z. Plasma-Enhanced Chemical Vapor Deposition of Polyperinaphthalene Thin Films. *Synth. Met.* **2008**, *158*, 425–429.
- (41) Nishio, S.; Fukumura, H.; Tamura, K.; Murata, J.; Kitahara, J.; Kan, T.; Matsuzaki, A.; Ando, N.; Hato, Y. Preparation of Polyperinaphthalenic Organic Semiconductive Nanoparticles by Excimer Laser Ablation and Their Application to Optic and Electronic Devices. *J. Laser Appl.* **2003**, *15*, 179–183.
- (42) Chen, J.; Zhang, J.; Zou, Y.; Xu, W.; Zhu, D. PPN (Poly-Peri-Naphthalene) Film as a Narrow-Bandgap Organic Thermoelectric Material. *J. Mater. Chem. A* **2017**, *5*, 9891–9896.
- (43) Ritter, C.; Muniz, R. B.; Latgé, A. Graphene Nanoribbon Molecular Sensor Based on Inelastic Transport. *Appl. Phys. Lett.* **2014**, *104*, 143107.
- (44) Jaiswal, N. K.; Kovačević, G.; Pivac, B. Reconstructed Graphene Nanoribbon as a Sensor for Nitrogen Based Molecules. *Appl. Surf. Sci.* **2015**, *357*, 55–59.
- (45) Akbari, E.; Yousof, R.; Ahmadi, M. T.; Kiani, M. J.; Rahmani, M.; Feiz Abadi, H. K.; Saeidmanesh, M. The Effect of Concentration on Gas Sensor Model Based on Graphene Nanoribbon. *Neural Comput. Appl.* **2014**, *24*, 143–146.
- (46) Abbas, A. N.; Liu, G.; Narita, A.; Orosco, M.; Feng, X.; Müllen, K.; Zhou, C. Deposition, Characterization, and Thin-Film-Based Chemical Sensing of Ultra-long Chemically Synthesized Graphene Nanoribbons. *J. Am. Chem. Soc.* **2014**, *136*, 7555–7558.
- (47) Chen, Z.; Zhang, W.; Palma, C.-A.; Lodi Rizzini, A.; Liu, B.; Abbas, A.; Richter, N.; Martini, L.; Wang, X.-Y.; Cavani, N.; Lu, H.; Mishra, N.; Coletti, C.; Berger, R.; Klappenberger, F.; Kläui, M.; Candini, A.; Affronte, M.; Zhou, C.; De Renzi, V.; del Pennino, U.; Barth, J. V.; Räder, H. J.; Narita, A.; Feng, X.; Müllen, K. Synthesis of Graphene Nanoribbons by Ambient-Pressure Chemical Vapor Deposition and Device Integration. *J. Am. Chem. Soc.* **2016**, *138*, 15488–15496.
- (48) Sakaguchi, H.; Kawagoe, Y.; Hirano, Y.; Iruka, T.; Yano, M.; Nakae, T. Width-Controlled Sub-Nanometer Graphene Nanoribbon Films Synthesized by Radical-Polymerized Chemical Vapor Deposition. *Adv. Mater.* **2014**, *26*, 4134–4138.
- (49) Sakaguchi, H.; Song, S.; Kojima, T.; Nakae, T. Homochiral Polymerization-Driven Selective Growth of Graphene Nanoribbons. *Nat. Chem.* **2016**, *9*, 57–63.
- (50) Chen, Z.; Wang, H. I.; Bilbao, N.; Teyssandier, J.; Precht, T.; Cavani, N.; Tries, A.; Biagi, R.; De Renzi, V.; Feng, X.; Kläui, M.; De Feyter, S.; Bonn, M.; Narita, A.; Müllen, K. Lateral Fusion of Chemical Vapor Deposited N = 5 Armchair Graphene Nanoribbons. *J. Am. Chem. Soc.* **2017**, *139*, 9483–9486.
- (51) Forrest, S. R. Ultrathin Organic Films Grown by Organic Molecular Beam Deposition and Related Techniques. *Chem. Rev.* **1997**, *97*, 1793–1896.
- (52) Yang, W.; Lucotti, A.; Tommasini, M.; Chalifoux, W. A. Bottom-Up Synthesis of Soluble and Narrow Graphene Nanoribbons Using Alkyne Benzannulations. *J. Am. Chem. Soc.* **2016**, *138*, 9137–9144.
- (53) Zhou, J.; Dong, J. Vibrational Property and Raman Spectrum of Carbon Nanoribbon. *Appl. Phys. Lett.* **2007**, *91*, 173108.
- (54) Vandescuren, M.; Hermet, P.; Meunier, V.; Henrard, L.; Lambin, P. Theoretical Study of the Vibrational Edge Modes in Graphene Nanoribbons. *Phys. Rev. B: Condens. Matter Mater. Phys.* **2008**, *78*, 195401.
- (55) Scholz, R.; Kobitski, A. Y.; Kampen, T. U.; Schreiber, M.; Zahn, D. R. T.; Jungnickel, G.; Elstner, M.; Sternberg, M.; Frauenheim, T. Resonant Raman Spectroscopy of 3,4,9,10-Perylene-Tetracarboxylic-Dianhydride Epitaxial Films. *Phys. Rev. B: Condens. Matter Mater. Phys.* **2000**, *61*, 13659–13669.
- (56) Tenne, D. A.; Park, S.; Kampen, T. U.; Das, A.; Scholz, R.; Zahn, D. R. T. Single Crystals of the Organic Semiconductor Perylene Tetracarboxylic Dianhydride Studied by Raman Spectroscopy. *Phys. Rev. B: Condens. Matter Mater. Phys.* **2000**, *61*, 14564–14569.
- (57) Simonov, K. A.; Vinogradov, N. A.; Vinogradov, A. S.; Generalov, A. V.; Zagrebina, E. M.; Mårtensson, N.; Cafolla, A. A.; Carpy, T.; Cunniffe, J. P.; Preobrajenski, A. B. Effect of Substrate Chemistry on the Bottom-Up Fabrication of Graphene Nanoribbons: Combined Core-Level Spectroscopy and STM Study. *J. Phys. Chem. C* **2014**, *118*, 12532–12540.
- (58) Teeter, J. D.; Costa, P. S.; Mehdi Pour, M.; Miller, D. P.; Zurek, E.; Enders, A.; Sinitskii, A. Epitaxial Growth of Aligned Atomically Precise Chevron Graphene Nanoribbons on Cu(111). *Chem. Commun.* **2017**, *53*, 8463–8466.
- (59) Yang, L.; Park, C.-H.; Son, Y.-W.; Cohen, M. L.; Louie, S. G. Quasiparticle Energies and Band Gaps in Graphene Nanoribbons. *Phys. Rev. Lett.* **2007**, *99*, 186801.
- (60) Kim, W.; Javey, A.; Vermesh, O.; Wang, Q.; Li, Y.; Dai, H. Hysteresis Caused by Water Molecules in Carbon Nanotube Field-Effect Transistors. *Nano Lett.* **2003**, *3*, 193–198.
- (61) Wang, H.; Wu, Y.; Cong, C.; Shang, J.; Yu, T. Hysteresis of Electronic Transport in Graphene Transistors. *ACS Nano* **2010**, *4*, 7221–7228.
- (62) Lipatov, A.; Varezchnikov, A.; Wilson, P.; Sysoev, V.; Kolmakov, A.; Sinitskii, A. Highly Selective Gas Sensor Arrays Based on Thermally Reduced Graphene Oxide. *Nanoscale* **2013**, *5*, 5426–5434.
- (63) Lipatov, A.; Varezchnikov, A.; Augustin, M.; Bruns, M.; Sommer, M.; Sysoev, V.; Kolmakov, A.; Sinitskii, A. Intrinsic Device-to-Device Variation in Graphene Field-Effect Transistors on a Si/SiO<sub>2</sub> Substrate as a Platform for Discriminative Gas Sensing. *Appl. Phys. Lett.* **2014**, *104*, 013114.
- (64) Voloshina, E. N.; Mollenhauer, D.; Chiappisi, L.; Paulus, B. Theoretical Study on the Adsorption of Pyridine Derivatives on Graphene. *Chem. Phys. Lett.* **2011**, *510*, 220–223.
- (65) Borini, S.; White, R.; Wei, D.; Astley, M.; Haque, S.; Spigone, E.; Harris, N.; Kivioja, J.; Ryhänen, T. Ultrafast Graphene Oxide Humidity Sensors. *ACS Nano* **2013**, *7*, 11166–11173.
- (66) Latif, U.; Dickert, F. Graphene Hybrid Materials in Gas Sensing Applications. *Sensors* **2015**, *15*, 30504–30524.

- (67) Mao, S.; Lu, G.; Chen, J. Nanocarbon-Based Gas Sensors: Progress and Challenges. *J. Mater. Chem. A* **2014**, *2*, 5573–5579.
- (68) Röck, F.; Barsan, N.; Weimar, U. Electronic Nose: Current Status and Future Trends. *Chem. Rev.* **2008**, *108*, 705–725.
- (69) Li, Z.; Askim, J. R.; Suslick, K. S. The Optoelectronic Nose: Colorimetric and Fluorometric Sensor Arrays. *Chem. Rev.* **2019**, *119*, 231–292.
- (70) Sysoev, V.; Kiselev, I.; Frietsch, M.; Goschnick, J. Temperature Gradient Effect on Gas Discrimination Power of a Metal-Oxide Thin-Film Sensor Microarray. *Sensors* **2004**, *4*, 37–46.